Computer Communications 201 (2023) 48–58

Contents lists available at ScienceDirect

Computer Communications

journal homepage: www.elsevier.com/locate/comcom

Empirical blockage characterization and detection in indoor sub-THz communications

Alexander Shurakov [a,b,*], Dmitri Moltchanov [c], Anatoliy Prikhodko [a,b], Abdukodir Khakimov [d], Evgeny Mokrov [d], Vyacheslav Begishev [d], Ivan Belikov [a,b], Yevgeni Koucheryavy [c], Gregory Gol'tsman [a,b]

[a] Moscow Pedagogical State University, Moscow, Russia
[b] National Research University Higher School of Economics, Moscow, Russia
[c] YL-Verkot Oy, Tampere, Finland
[d] Peoples' Friendship University of Russia (RUDN University), Moscow, Russia

ARTICLE INFO

Keywords:
6G
Sub-THz communication
Indoor deployment
Blockage metrics
Blockage detection algorithm

ABSTRACT

The next step in the last mile wireless access is utilization of the terahertz (THz) frequency band spanning from 0.1 to 3 THz, specifically, its lower part (up to 300 GHz) also known as sub-THz frequencies. At these frequencies, communication systems can offer tens of consecutive gigahertz potentially allowing to further improve access rates at the air interface to dozens of gigabits-per-second. However, the effect of blockage evident already at millimeter waves is expected to be much more pronounced at frequencies beyond 100 GHz. In this paper, we empirically investigate the characteristics of the human body blockage by conducting a measurement campaign at carrier frequency of 156 GHz in the indoor environment. We concentrate on both mean attenuation and time-related metrics of the blockage process including the signal fade and rise times, and blockage duration. For a point-to-point transmission over a distance of 3–7 m, we find that the mean attenuation is in the range of 8–15 dB depending on the line-of-sight (LoS) height and the transmitter-to-receiver (Tx-to-Rx) distance. The blockage duration varies within 5%–10% for different Tx-to-Rx distances (with corresponding nominal values of 360–390 ms) while the signal rise and fall times gradually increase from 60 to 100 ms with the Tx-to-Rx distance growth and remain unchanged for different LoS heights. The developed blockage detection algorithm allows one to identify the blockage occurrence with a probability of 0.96–0.98 within 1–3 ms at the channel sampling rate of 500 ksample/s and 3–5 event/s of false alarm rate which is on par with modern machine learning based approaches.

1. Introduction

As the standardization process of the New Radio (NR) access technology for millimeter waves is almost over, the researchers started investigating the use of higher frequencies and initiated intensive mastering of the terahertz (THz) band covering 0.1–10 THz [1]. Its lower part (up to 300 GHz) is often referred to as the sub-THz frequency range. At the moment, THz wireless communication is identified as a promising technology for the sixth generation (6G) networks.

The adoption of THz communication should provide continuous bands of up to several tens of gigahertz thus leading to an order of magnitude improvement in the data rates. The first steps in this direction have already been made with the ratification of IEEE 802.15.3d standard providing 100 Gbps at the air interface for stationary and semi-stationary devices [2]. However, to enable truly mobile cellular systems numerous fundamental and technical challenges have to be resolved.

THz communication potentially suffers from high propagation losses including those due to the atmospheric water vapor absorption [3]. To partly overcome this issue, THz antenna arrays are expected to feature hundreds or even thousands of elements forming extremely directional radiation patterns of just a few degrees of beamwidth [4]. The latter not only compensates the severe path and absorption losses at THz frequencies, but notably reduces the impact of interference in future wireless networks [5].

The extremely directive nature of THz data transmission, however, has certain consequences. First of all, performance of the communication system is heavily affected by micromobility such as shakes

* Corresponding author at: Moscow Pedagogical State University, Moscow, Russia.
E-mail addresses: alexander@rplab.ru (A. Shurakov), dm@yl-verkot.com (D. Moltchanov), anprihodko@hse.ru (A. Prikhodko), khakimov-aa@rudn.ru (A. Khakimov), mokrov-ev@rudn.ru (E. Mokrov), begishev-vo@rudn.ru (V. Begishev), ibelikov@hse.ru (I. Belikov), yk@yl-verkot.com (Y. Koucheryavy), goltsman@rplab.ru (G. Gol'tsman).

https://doi.org/10.1016/j.comcom.2023.01.017
Received 21 June 2022; Received in revised form 19 October 2022; Accepted 19 January 2023
Available online 25 January 2023

and rotations even when a user is in the stationary position [6]. The ultimate impact of micromobility is spontaneous degradation of a signal-to-noise ratio (SNR) leading to outages [7,8]. In addition, the data transmission also suffers from blockage by dynamic objects. The blockage issue is expected to be much more severe compared to that observed at millimeter waves.

The human body blockage process at frequencies beyond 100 GHz has been insufficiently studied so far, see Section 2. There are several studies already proposing mathematical models for blockage process, capacity, and outage performance of future 6G THz systems. Yet, a little is known in terms of attenuation induced by the blockage and its temporal characteristics. Those include the blockage duration and the time it takes for a signal to fade to a blocked state and rise back after the blockage is completed. The latter two are of special interest for designing efficient beamsearching algorithms for THz systems, where the beamwidth is expected to be much smaller compared to that conventionally employed below 100 GHz. These timings may also impose additional constraints on the design of the medium access control protocols for 6G systems.

To timely avoid outage, blockage detection algorithm has to be utilized. Up to date, a number of these algorithms has been proposed, mainly, based on supervised machine learning (ML) techniques, see Section 2 for review. However, the performance of these algorithms has been conventionally assessed by utilizing the blockage detection probability leaving the detection delay and false alarm rate of the algorithms aside. Despite the fact that machine learning algorithms can provide high blockage detection probability reaching 0.9–0.95, they are naturally associated with training delays and high implementation complexity leaving the channel unattended for long periods of time. Thus, there is a need for a simple blockage detection algorithm having comparable accuracy.

In this paper, we are filling the aforementioned gaps by comprehensively characterizing blockage for the first time in the THz band, at carrier frequency of ~156 GHz. To this aim, having in mind AR/VR use-cases in the indoor environment we carry out a large scale indoor measurement campaign for different distances between transmitter (Tx) and receiver (Rx), different Tx and Rx heights as well as different offsets to the blocker crossing the line-of-sight (LoS) path. Collecting one hundred samples for each configuration of the measurement setup, we report not only on the mean values of sought metrics of interest, but on their distributions as well. We concentrate on attenuation brought by blockage of the LoS path, and also on the time-related metrics such as blockage duration, signal rise and fall times. We provide a quantitative comparison of our findings with results reported earlier for 28/60/72 GHz. We further proceed with proposing blockage detection algorithms based on a change-point statistical test. And finally, we compare proposed algorithms with those reported in the literature in terms of three key parameters: (i) detection probability, (ii) detection latency, and (iii) false blockage detection rate (false alarm rate).

The main contributions of our work are:

- *overall experimental data:* empirical measurements campaign of human body blockage process in the indoor environment at carrier frequency of 156 GHz;
- *blockage mean attenuation:* for a point-to-point transmission over a distance of 3–7 m, blockage-induced attenuation is in the range of 8–15 dB depending on the LoS height and is higher for smaller distance;
- *blockage temporal metrics:* blockage duration is independent of the Tx-to-Rx and blocker-to-Rx distances and is in the range of 360–390 ms, rise and fall times gradually increase with the Tx-to-Rx distance growth and remain unchanged for a given LoS height;
- *blockage detection:* the developed algorithm allows one to identify the blockage occurrence with a probability of 0.96–0.98 within 1–3 ms at the channel sampling rate of 5×10^5 sample/s and 3–5 event/s of false alarm rate.

The rest of the paper is organized as follows. In Section 2 we overview the related work in the field. We introduce the measurement equipment and characterize the setup of experiments in Section 3. In Section 4, we quantitatively characterize the blockage. Then, in Section 5 we provide blockage detection algorithms and their numerical assessment. Conclusions are drawn in the last section.

2. Related work

In this section, we provide a review of the studies performed so far for blockage characterization and detection at millimeter waves and in the THz band.

2.1. Blockage characterization

In spite of several studies already reporting propagation specifics at frequencies above 100 GHz, the results on blockage process dynamics are still scarce. The study in [9] provides an overview of propagation and penetration loss measurements at 140 GHz for various building materials and beamwidths of 8 degrees. However, the authors do not report blockage process characteristics. The authors in [10,11] explicitly report the attenuation values for carrier frequency of 300 GHz for vehicular blockage. However, these results cannot be extrapolated to the human body blockage in the indoor environment.

Several authors investigate the transparency properties of the materials [12–14]. The paper [12] investigates the penetration and fall of the signal level for different materials in the THz band, and more precisely for a frequency of 140 GHz. Blockage measurements were made for the following materials: clear glass, glass door, drywall, and drywall with whiteboards of different thicknesses. The drop in the signal level in case of a blocking drywall with whiteboard was 16.69 dB, and for a glass with a thickness of 0.6 cm it was 8.24 dB. In [13], the authors carry out measurements at 4 frequencies, 2 of which belong to the THz band. The configuration of the experimental setup has the following properties: antenna gain is 21 dBi, beamwidth is 15°, and the Tx-to-Rx distance from 0.2 to 0.7 m. Thus, the signal attenuation level for plywood is 16.068 dB. Similar results have been reported in [14].

In addition to the studies covering the properties of materials, several authors developed analytical models by accounting for key features of blockage in the THz band. Specifically, the authors in [15] deduce the probabilistic function of blocking a terahertz signal with several blockers in the indoor scenarios. In the paper, the essential parameters of blockage and the blockers are summarized as the mutual arrangement of Rx and Tx (in a pocket or in hand), average height, antenna parameters, and room dimensions. Based on the average value of blockage probability, the authors calculated the average number of people in the room with LoS for this scenario. They studied the performance improvements in terms of coverage due to the utilization of more than a single antenna. The study in [16] investigates the average bandwidth at terahertz frequencies in the presence of blockage induced by a human body. The authors find the optimal number of excess points in the room to maximize the probability of coverage for a given threshold of signal to interference and noise ratio (SINR). For that, the authors recreate the antenna beam model for each access point, thereby obtaining a maximum speed of 30 Gbps per square meter. For dynamic blocking caused by human movement in three-dimensional space, [17] offers a flexible analytical framework to deduce the optimal base station (BS) locations to prevent blockages. The authors find that increasing the directivity of the antennas at the BS results in better coverage than increasing the directivity of user equipment (UE). The study in [8] reports on the fraction of time in outage and capacity in presence of both blockage and user micromobility impairments.

By summarizing the current state in blockage characterization and modeling, we can see that this effect is going to play a critical role in future 6G THz communication systems. By extrapolating the data available on penetration of THz signal through various materials and

measurement campaign for vehicular communication, we also deduce that it is going to be much stronger as compared to millimeter waves and may more frequently lead to the outage as often assumed in mathematical models reported above. However, there is still no rigorous characterization of the human body blockage process in the THz band.

2.2. Blockage detection

Blockage detection has received significantly less attention in the recent literature. In general, the proposed algorithms can be divided into offline and online ones. The former ones are those allowing to precisely identify various quantities in the blockage process, e.g., rise, fall, duration of blockage. They may rely upon the full statistics available to analysts and for this reason usually more precise as compared to the online algorithms. The aim of the latter type of algorithm is to provide a way to detect blockage in real-time, e.g., change modulation and coding scheme (MCS) prior to signal fade. From this point of view, online blockage detection methods are inherently limited to the statistics available prior to the current time instant and, at the same time, pose strict requirements in terms of detection latency and detection accuracy.

In [18], the authors proposed an online blockage detection algorithm based on Deep Neural Network (DNN) with ReLu activation function for carrier frequency of 48 GHz. As a metric of interest, they utilized the NR frame loss rate. The numerical evaluation campaign has been carried out using the system-level simulations and their results reveal that for blocker's speed of 2 m/s the frame loss rate is just 4%. However, no analysis has been carried out as to what part of potential losses can be attributed to the functionality of the algorithm itself. The authors in [19] also utilize the ML approach specifically, DNN, to detect blockages caused by blockage and self-blockage. Specifically, the DNN algorithm is used to detect blockage at carrier frequency of 30 GHz with a channel bandwidth of 100 MHz. The accuracy of the utilized DNN-based algorithm was reported in the range of 0.9–0.95 in terms of successful blockage detection. However, to achieve this accuracy, the DNN algorithms have been trained by utilizing more than 16000 data points with blockage time instants identified manually.

The study in [20] also investigates blockage detection at millimeter waves, specifically at 60 GHz. The considered scenario corresponds to the case of multiple human blockage, i.e. when a LoS path is blocked by several humans simultaneously. Similar to the previously reviewed studies, the ML approach is proposed by the authors. Specifically, they utilize a long short-term memory (LSTM) neural network to dynamically adjust the detection function. The reported accuracy in terms of blockage detection probability approaches 0.97 outperforming the method proposed in [19]. A unique feature of the study is the consideration of the blockage by different parts of the human body, depending on the height of LoS path. This property is explicitly accounted for in LTSM parameterization and is shown to directly affect the detection accuracy.

There are also studies that explore blockage phenomenon at lower frequencies, more precisely for sub-6 GHz channels. They also primarily utilize ML methods for blockage detection. Specifically, the study in [21] addresses this case by utilizing DNNs. In spite of having much milder attenuation at these frequencies ranging from 3 to 6 dB [22], the reported results for blockage detection probability reach 0.98. This is achieved by adding more intermediate layers to the neural network as compared to [20].

An in-depth study of human blockage detection has been carried out in [23]. Even though the authors also advocated the use of the ML approach, they also investigated in detail the received signal strength (RSS) signatures occurring prior to blockage. Based on this observation, they propose to detect not the actual drop in the RSS, but the signature prior to the blockage providing probabilistic estimates that a blockage will follow. This technique allows one to quickly respond to the blockage providing a time budget for the change of the MCS.

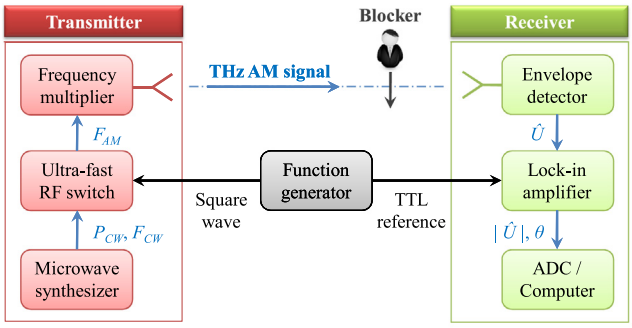

Fig. 1. Schematic diagram of a THz transceiver.

Summarizing the blockage detection review, we observe that there are no studies addressing blockage detection in the THz band so far. While there might not be a drastic difference between blockage profiles compared to those observed at millimeter waves, the proposed online blockade detection algorithms do not address two critical metrics of interest — detection latency and false alarm rate. The former is of special importance for the use of the algorithm in practice, when the change of the MCS scheme has to be done in advance to protect from blockage. The false alarm rate, on the other hand, is another critical measure for the online blockage detection algorithm characterizing its accuracy along with blockage detection probability. Finally, most of the approaches consider the problem as a black-box by directly applying and testing the performance of ML algorithms.

3. Experimental setup

In this section, we introduce our measurement setup, experiment configurations, and present details on acquisition, calibration and post-processing of experimental data.

3.1. Measurement setup

In our experiments, Tx is a solid state THz source providing up to 120 mW of output power over the frequency range of 134–158 GHz. Referring to Fig. 1, a CW signal produced by a microwave synthesizer is fed into a frequency multiplier through an ultra-fast RF switch. The switch is driven by a square wave from a synthesized function generator which results in AM frequency of 100 kHz. The carrier frequency is set to 156 GHz with a corresponding power of 90 mW. The AM signal is delivered to free space through a pyramidal horn, which has a gain of 25 dB and a half power beamwidth of 10°. After passing a distance of 3–7 m, the signal is received. Rx makes use of a Schottky diode enveloper detector equipped with a horn antenna identical to that of Tx, the antennas are coaxially aligned. Response voltage of the envelope detector is registered by a lock-in amplifier synchronized with the solid state THz source via TTL reference. Voltages from the lock-in amplifier amplitude and phase analog output channels are acquired by a digital oscilloscope and further transferred to a computer. The lock-in amplifier is operated with a time constant of 30 μs while the time resolution of the oscilloscope is set to 50 μs.

3.2. Experiment configurations

An illustration of the measurement setup described is provided in Fig. 2. We conducted a series of experiments with a mutual arrangement of Tx, Rx, and a blocker as appears in Table 1. The corresponding considered blockage configurations are illustrated in Fig. 3. The blocker was crossing the LoS path with an average velocity of ~3.5 km/h. Ambient conditions were registered using regular appliances. During the experiments, we observed small changes in ambient temperature,

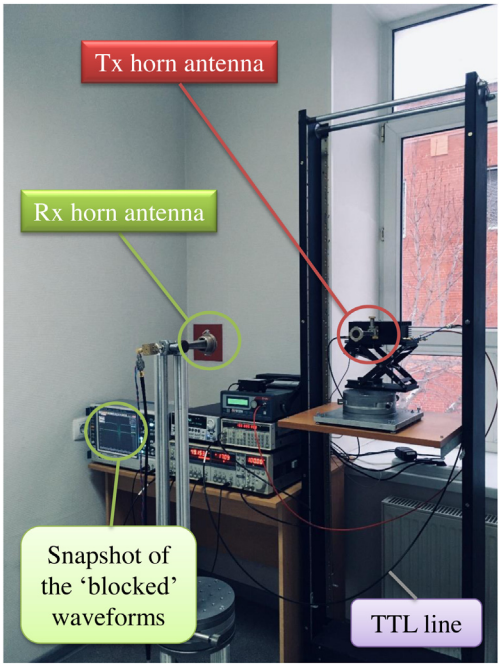

Fig. 2. Illustration of a THz measurements setup.

T_{AMB}, and relative humidity, RH: $T_{AMB} = 23 \pm 0.2$ °C and $RH = 23.9 \pm 0.6$ %. The experiments were conducted in an empty hall with linear dimensions of 7.5 m × 2.4 m × 3 m (length × width × height).

3.3. Calibration and postprocessing

Before statistical processing, we present our experimental data in a form of the power-vs-time waveform. This requires auxiliary measurement of the envelope detector responsivity and linearity curve. The measurement is carried out with the aid of the solid state THz source equipped with a voltage-controllable waveguide attenuator and a precision waveguide power meter. Response voltage of the envelope detector registered by the lock-in amplifier (see Fig. 1 for details) is accordingly converted into a THz power incident on the aperture of the Rx horn antenna. It is worth mentioning that the power values within each waveform obey Gaussian distribution with a high degree of accuracy.

The envelope detector is originally developed by us [24] for precision power measurements in the frequency range of 110–170 GHz. It has a return loss as high as 25–30 dB and is designed for input power levels from 1 nW up to 1 mW. This is achieved at the expense of the detector responsivity, which equals 14.3 V/W at 156 GHz.

4. Blockage characterization

In this section, we present our numerical results on the explored characteristics including the mean attenuation level, blockage rise and fall times, and their duration. Then, we proceed characterizing the cumulative distribution functions (CDF) of the investigated metrics. Further, we report on the path loss model in the considered part of the THz band.

4.1. Blockage detection

To report the metrics of interest, we employ the following offline blockage detection algorithm. Specifically, let t_B, t_F and t_R be the signal blockage, fall, and rise times, respectively, as shown in Fig. 4, where two typical RSS time series are illustrated for two different

Table 1
Experimental setup configurations.

Config #	h [m]	x [m]	d [m]	d' [m]
1	1.33	3	1.5	1.5
2	1.33	5	1.5	3.5
3	1.33	5	2.5	2.5
4	1.33	5	3.5	1.5
5	1.33	7	1.5	5.5
6	1.33	7	3.5	3.5
7	1.33	7	5.5	1.5
8	1.65	3	1.5	1.5
9	1.65	5	1.5	3.5
10	1.65	5	2.5	2.5
11	1.65	5	3.5	1.5
12	1.65	7	1.5	5.5
13	1.65	7	3.5	3.5
14	1.65	7	5.5	1.5

Here h is the vertical position of Tx and Rx relative to the floor (i.e. LoS height), x is the distance between Tx and Rx, d is the distance between Tx and a blocker, d' is the distance between a blocker and Rx.

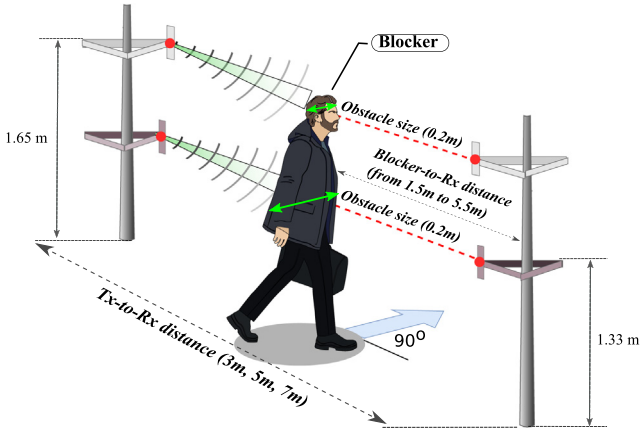

Fig. 3. Illustration of the considered scenario.

configurations of experimental setup. Here, we assume that the overall time series is available for analysis as opposed to the online blockage detection considered in Section 5 that considerably simplifies the procedure.

We start with the overall impairment time induced by a blocker, i.e., $t_B + t_F + t_R$. To identify it, we first detect the global minimum over the entire time series, $L_{\min}$. Then, we proceed with determining the minimum value for the non-blocked state, $L_{\min,nB}$. We note that the experiments were carried out such that the time interval for the non-blocked state of the THz signal transmission is at least three times larger than that of the blocked state. Thus, one can approximate the sought variable by (a) identifying a 25% long time interval in the entire power-vs-time series and (b) further finding the value of $L_{\min,nB}$ in this interval. This interval occurs prior to the blockage if $L_{\min}$ is observed in the second half of the time series and is after it if $L_{\min}$ is in the first half.

Then, we proceed with shortening the identified interval point by point from both ends towards the center and comparing the attenuation levels with a predefined threshold, Δ. We choose $\Delta = \delta E[L]$, where $E[L]$ is the mean in the non-blocked state and δ is the user-defined parameter. Once a point crosses δ, it signals the beginning or the end of the overall period of signal degradation of duration $t_B + t_F + t_R$.

Once the overall period $t_B + t_F + t_R$ is detected, we proceed to isolating the signal fall and rise times. Accounting for the fact that the actual blockage duration is much greater than the signal fall and rise times, we divide the overall blockage period into three non-overlapping periods of the same length and determine the maximum value, $L_{\max}$, of the middle interval. Then, we again proceed to shortening the identified

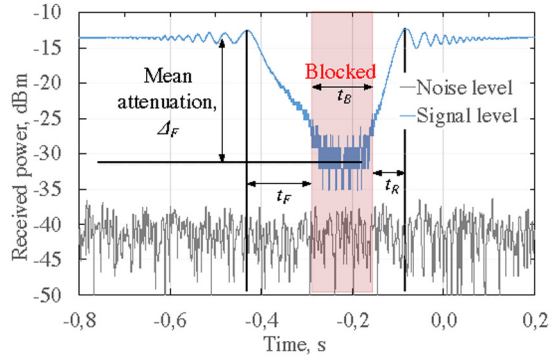

(a) Configuration #4 of mutual arrangement of Tx, Rx and a blocker: $h = 1.33$ m, $x = 5$ m, $d' = 1.5$ m (see Tab. 3.3)

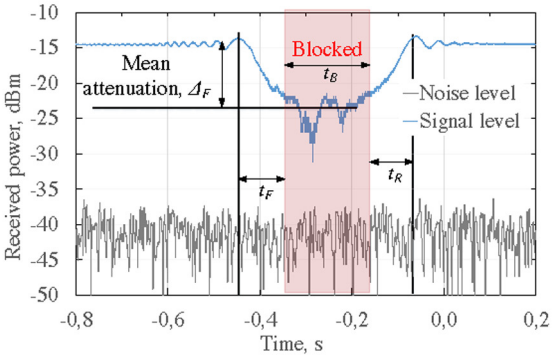

(b) Configuration #9 of mutual arrangement of Tx, Rx and a blocker: $h = 1.65$ m, $x = 5$ m, $d' = 3.5$ m (see Tab. 3.3)

Fig. 4. Experimental time series illustrating the THz blockage dynamics.

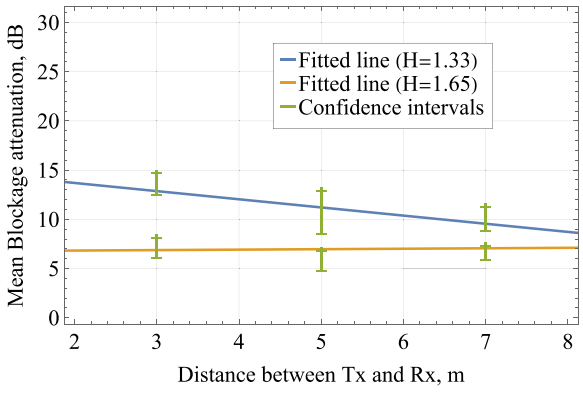

(a) Mean value

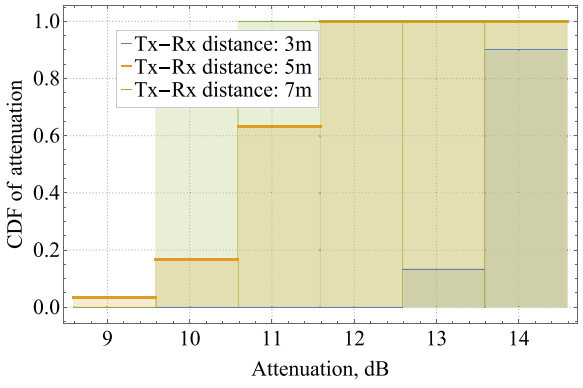

(b) CDF

Fig. 5. Attenuation when blocker crosses LoS at the middle point.

intervals from both ends towards the center and comparing the attenuation levels with $L_{\max}$. The first points, L_S and R_S, matching $L_{\max}$ identify the beginning and the end of the blockage period. Therefore, we have

$$\begin{cases} t_F = L_S - t_{B,S} \\ t_B = T_{B,E} - t_{B,S} \\ t_R = R_S - t_{B,E} \end{cases}, \tag{1}$$

where $t_{B,S}$, and $t_{B,E}$ are the beginning and the end of the impairment period identified at the previous stage.

4.2. Blockage attenuation

We start with blockage attenuation characterization. To this aim, Fig. 5 shows the resulting data, confidence intervals, and mean attenuation as a function of the distance between Tx and Rx. Here, blocker crosses LoS at the midpoint between communicating entities which correspond to 6 cases with $d = d' = 1.5, 2.5, 3.5$ m for the considered distances $x = 3, 5, 7$ m, respectively (see Table 1). First of all, as one may observe, the blockage attenuation is much smaller as compared to that reported for the millimeter wave systems in outdoor deployment scenarios (15–25 dB in [25–27]) and varies between 8 and 15 dB. This difference between different Tx-to-Rx distances is also clearly evident in terms of both the attenuation mean value and CDF demonstrated in Figs. 5(a) and 5(b), respectively. One of the plausible explanations is the difference in the considered scenarios. While the studies reported to date mainly concentrated on cellular communication between BS and UE, here we consider D2D scenario. In the former case, due to the difference between UE and BS heights only those blockers that are quite close to the Rx may block the LoS path. Furthermore, the link distance is much higher. In our D2D communication scenario, not only the link distance is comparable to the distance between the blocker and Rx, but the latter may also significantly affect the RSS.

By analyzing the data presented in Fig. 5(a), we note that the blockage attenuation behavior heavily depends on the LoS height. Specifically, for a high LoS height $h = 1.65$ m corresponding to the typical height of VR helmets (head height), we observe constant attenuation across all the considered distances of approximately 8 dB. Contrarily, at $h = 1.33$ m (chest height), the attenuation is clearly (i) higher than at the head level and (ii) distance-dependent starting from approximately 15 dB at $x = 3$ m and lowering down first to 12 dB at $x = 5$ m and then to 10 dB at $x = 7$ m. The first observation is explained by the fact that, geometrically, the chest produces much wider blockage area along vertical as compared to the head at all the distances. Lowering of attenuation at bigger Tx-to-Rx distances is due to the increase in beam areas produced by the Tx and Rx horn antennas at the blocker position. Moreover, diffraction effects are the position-dependent and cannot be completely neglected. These latter observations are drastically different from the conventional assumption that the human blockage induced attenuation remains constant as reported in, e.g. [25–27], and commonly taken in mathematical modeling both at millimeter waves and in the THz band [28].

To better illustrate the aforementioned conclusions, we now proceed with evaluating blockage induced attenuation for different distances from Rx to blocker, illustrated in Fig. 6. As one may observe, the considered Rx-to-blocker distances do not impact on the induced attenuation drastically as all the deviations stay well within 1–2 dB with the notable exception of 1.5 m distance at 1.33 m LoS height. We

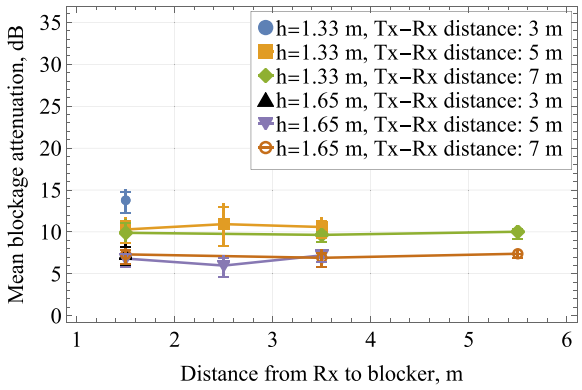

Fig. 6. Mean blockage attenuation for different blocker-to-Rx distances.

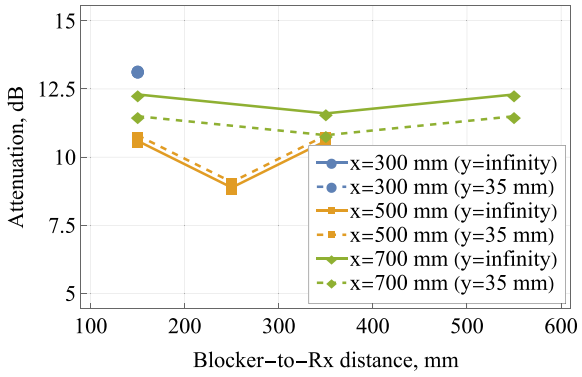

Fig. 7. FEM-simulated attenuation as a function blocker-to-Rx distance.

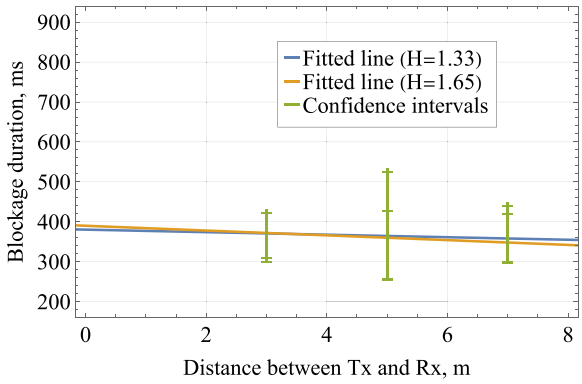

(a) Mean value

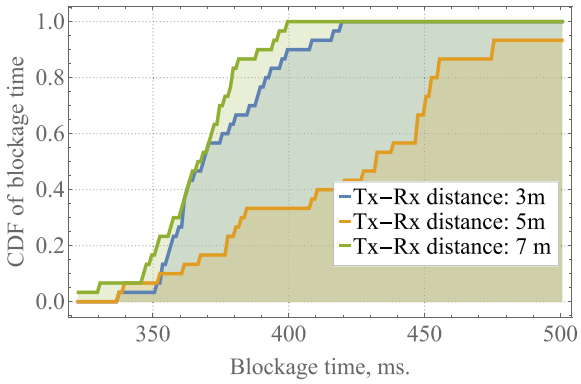

(b) CDF

Fig. 8. Blockage duration when blocker crosses LoS at the middle point.

believe that this is mainly due to the fact that the number of Fresnel zones in obstacle, F, decreases from 13.3 to 3.6 in our experiments in response to the increase of blocker-to-Rx distance from 1.5 to 5.5 m. This correspondingly results in enhancement of effects due to Fresnel diffraction.

To further justify observed trends in experimentally obtained dependencies of attenuation on blocker-to-Rx distance, we perform an electromagnetic (EM) simulation. The EM simulation is implemented with the aid of a finite element method (FEM) in COMSOL Multiphysics. To achieve desired time efficiency for available computation capacity, we create a set of 2D EM models in 1:10 scale. The radiation wavelength is 2 mm. Geometry of the Tx and Rx horns is identical to the cross section of the pyramidal horns used in the experiments, and the distance between them x varies from 300 to 700 mm. The simulation area between the horns is $x \times 110$ mm (length × width). The blocker is presented by a 20 mm long segment. For such a setup, F is in the range of 0.36–1.33, and, therefore, Fresnel diffraction is expected to be slightly more pronounced compared to that observed in the conducted experiments. Evaluation of diffraction effects is maintained via dual-regime calibration of Tx-to-Rx propagation loss, L_{REF}.

Fig. 7 provides simulated attenuation profiles for 2 different L_{REF} acquired, when the blocker is at the middle of the LoS path and is displaced from it along perpendicular by $y = 35$ mm and $y = \infty$. We observe the appearance of either increase (Fig. 7, $x = 500$ mm) or decrease of attenuation (Fig. 7, $x = 700$ mm) upon insertion of an obstacle aside of the LoS path. And no significant effect is observed for $x = 300$ mm. Moreover, both nominal values and overall trends in the attenuation profiles statistically agree with the experimental results for $h = 1.33$ m, but not for $h = 1.65$ m. This finding is consistent with the fact that geometry of the blocker (see Fig. 3) results in significant difference in blockages of transmitted beams at different heights. Indeed, almost the entire upper half of the beam is open for all the experiment configurations with $h = 1.65$ m, when blocker is at a midway across the beam, while its lower part is blocked by a 20 cm wide obstacle at the half-beam center. At $h = 1.33$ m, however, a 20 cm wide central part of the beam is completely blocked along vertical. And this is very similar to the geometry of our 2D EM models of the experiment configurations.

4.3. Time-dependent metrics

Having reported the results on blockage induced attenuation, we now proceed to characterizing time-related metrics including: (i) blockage duration, (ii) time to drop from non-blocked to blocked state — fall time, and (iii) time to rise from blocked to non-blocked state — rise time. We start with the former metric, whose mean values and CDFs are illustrated in Figs. 8(a) and 8(b), respectively, as a function of the distance between Tx and Rx for a blocker crossing the midpoint of the link.

By analyzing the data presented in Fig. 8, one may observe that the statistical characteristics of the blockage duration are almost independent of the Tx–Rx link distance and LoS height. We specifically note that the mean reported in Fig. 8(a) for the LoS height of 1.33 m remains firmly constant at 380 ms for all the distances. For the LoS height of 1.65 m, there is a slight decrease in the mean blockage duration from observed 370 ms at $x = 3$ m to 350 ms at $x = 7$ m. Nevertheless, this produced just a 5% of difference. This difference is further highlighted in Fig. 8(b).

Further, Fig. 9 demonstrates mean blockage duration as a function of different blocker-to-Rx distances, where d is Tx-to-Rx distance. Here, we learn that for all Tx-to-Rx distances and any blocker-to-Rx distance the results remain steady. Higher variability is observed for 1.33 m Tx and Rx heights and Tx-to-Rx separation distances of 3 m and 5 m.

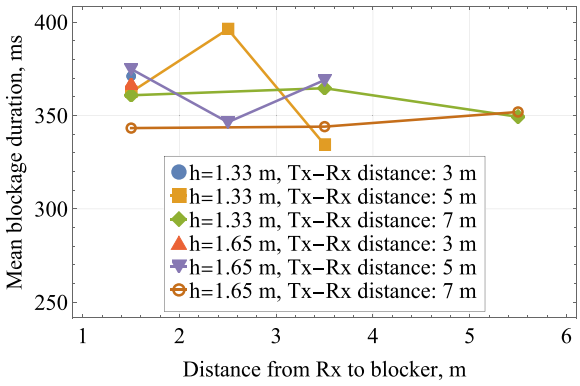

Fig. 9. Mean blockage duration for different blocker-to-Rx distances.

There are also slight differences in absolute values depending on the LoS height. Specifically, for $h = 1.65$ m (head level) blockage duration is slightly higher than those observed for $h = 1.33$ m. For example, for $x = 7$ m there is a 20 ms difference for all considered blocker-to-Rx distances. We note the relative difference between the reported values is 5%–10% which is much greater than the mean values in the range 330–370 ms. Thus, these differences will not affect blockage events but do affect blockage duration.

Now, we are in a position to proceed with characterizing fall and rise times, where the former is of critical importance for blockage detection algorithms considered in what follows. To this aim, Fig. 10 provides the mean values and CDFs of fall and rise times for considered Tx-to-Rx distances and blocker crossing the midpoint of LoS. By analyzing the results presented in Figs. 10(a) and 10(b), one may observe that both fall and rise times increase as a function of the distance potentially making it more feasible to timely detect blockage events. The absolute difference between the reported means is insignificant and lies within 2%–4% of the demonstrated values (e.g., 60 ms for $x = 3$ m, 80 ms for $x = 5$ m and 100 ms for $x = 7$ m for fall times). Notably, both fall and rise times have similar form of CDFs as illustrated in Fig. 10(c) and, in general, the mean rise time is 5%–10% longer than the fall time.

4.4. Propagation model

We now report the path loss model in the considered band. The general structure of the propagation model in decibel scale can be written by [29]

$$L(x) = y_1 \log_{10} x + 20 \log_{10} f_c + y_2 + I_B L_B(x, d), \tag{2}$$

where f_c is the carrier frequency in GHz, x is the distance between the THz BS and the UE, I_B is the indicator of the blockage event ($I_B = 1$ when blocked and $I_B = 0$ otherwise), $L_B(x, d)$ is the blockage induced attenuation at distance x between Tx and Rx and separation distance of d between Tx and blocker, y_1 and y_2 are some parameters that are usually determined via field measurements [30]. Note that the path loss in (2) can be represented in the linear scale by utilizing the model in the form of $z_1 x^{z_2}$, where z_1 and z_2 are the propagation coefficients, i.e.

$$z_1 = y_1/10,\ z_2 = 10^{2 \log_{10} f_c + y_2/10 + I_B L_B(x,d)/10}. \tag{3}$$

Note that the THz band is known to be affected by atmospheric absorption as discussed in [3,31]. However, at the considered frequency and owing to rather limited communication distances in the indoor environment the impact of this phenomenon is negligible. Thus, in what follows, we will look for a propagation model accounting for blockage as in (2).

We first need to identify coefficients y_1 and y_2. To aim, we utilize the data in non-blocked conditions to determine the fitted propagation model using the mean squared error (MSE) estimator. The results of the fitted model are shown in Fig. 11, where the identified coefficients are: $y_1 = -21.5604$ and $y_2 = -252.172$ dB for the LoS height of 1.35 m and $y_1 = -22.04$ and $y_2 = -251.704$ dB for the LoS height of 1.65 m. Averaging over the two considered LoS heights allows to identify the following propagation model

$$L(x, h) = 22.8 \log_{10} x + 20 \log_{10} f_c + 251 + \\ + I_B L_B(x, h), \tag{4}$$

where $L_B(x, d)$ depends on the Tx-to-Rx distance and LoS height, but is independent of Tx-to-blocker or blocker-to-Rx distance, that is

$$L_B(x, h) = \begin{cases} 15 \text{ dB}, & h = 1.33 \text{ m}, 1.65 \text{ m}, x \le 3 \text{ m} \\ 10 \text{ dB}, & h = 1.33 \text{ m} \\ 8 \text{ dB}, & h = 1.65 \text{ m} \end{cases}. \tag{5}$$

5. Blockage detection

In this section, we develop a novel blockage detection algorithm and evaluate its performance using the real measurement data. We also discuss the application and limitation of blockage detection.

5.1. Blockage detection algorithms

The detection of blockage is critical to avoid outages caused by human blockage events when utilizing 3GPP multiconnectivity functionality [32]. However, it is only useful when the blockage is detected way ahead of its actual occurrence, i.e. in a much smaller time than 25 ms as we have observed in the previous section. Similarly, detection of rise time instants may also be important to timely switch to a link with better signal quality. In this section, we proposed and evaluate blockage detection mechanisms and assess the requirements imposed on assessing channel quality to timely detect blockage situations.

Detecting abrupt changes in the RSS statistics such as those caused by blockage can be attributed to the class of change-point detection algorithms [33]. For detecting a blockage in the RSS time series the following interpretation of causes of deviation is taken. We assume that common causes of RSS stochastic behavior are small-scale changes in the UE locations of positions of objects in the channel causing the fading phenomenon [29]. Blockage causes the so-called special causes of deviations to be detected by the algorithm. For the considered algorithms below, the common following procedure is utilized. Once the algorithm starts, it utilizes K observations to parameterize its internal parameters. Once (if) blockage is falsely detected, we skip the next M data points, and initiate the algorithm again.

Assume that k observations $\{\xi_i, i = 0, 1, \dots\}$ of a certain stochastic process have the same distribution F_0. In general, the change-point statistical test refers to testing the null hypothesis, H_0, that a currently observed observation k has distribution F_0 against alternative hypothesis, H_1, that this observation has distribution F_1, i.e.

$$H_0 : F_{\xi_k} = F_0,\ H_1 : F_{\xi_k} = F_1, \tag{6}$$

where F_{ξ_k} is the distribution of observation k.

The latter case represents situation, when a change occurs in a distribution and can be rewritten as

$$H_0 : F_{\xi_k} = F_0,\ i = 1, 2, \dots, k, \\ H_1 : F_{\xi_k} = \begin{cases} F_0 = 0, 1, \dots, k-1, \\ F_1 = k. \end{cases} \tag{7}$$

It is often assumed that distributions F_0 and F_1 are known except for some parameters of F_1. In our case the form of distributions F_0 and F_1 and parameters of F_0 are known in advance (can be estimated from statistical data) and the unknown parameter is the mean value of F_1.

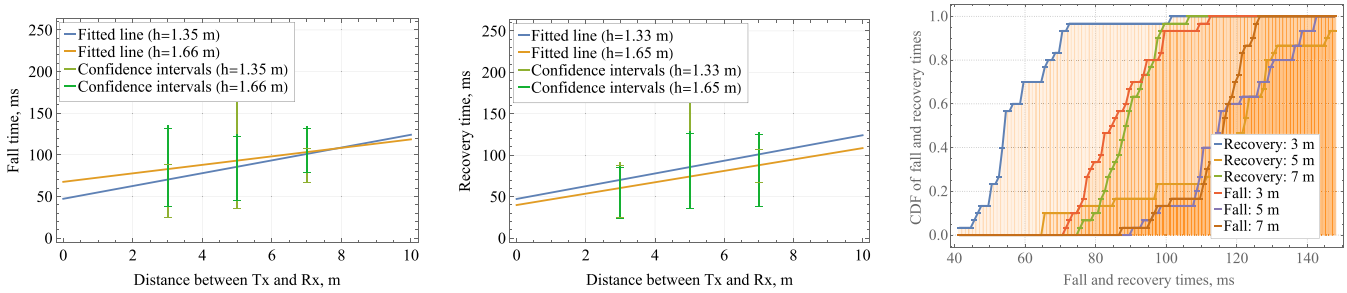

(a) Fall time (b) Rise time (c) Fall and rise time

Fig. 10. Mean values and CDF of fall and rise times when blocker crosses LoS at the middle point.

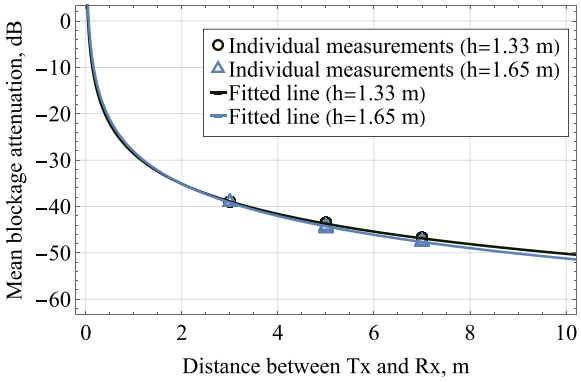

Fig. 11. Propagation model at 156 GHz.

Therefore, the task is to detect change in the mean RSS value resulting in the following test

$$H_0 : E[\xi_i] = \mu_0,\ i = 0, 1, \dots, k,$$
$$H_1 : E[\xi_i] = \begin{cases} \mu_0,\ i = 0, 1, \dots, k-1, \\ \mu_1,\ i = k, \end{cases} \tag{8}$$

where μ_0, μ_1 are the mean values prior and after the change.

5.2. The proposed approach

Consider the time series $\{\xi_i, i = 1, 2, \dots\}$ of the received signal strength measurements. The task is to determine the time instant of the beginning of the abrupt downward change in the mean value of the observed process.

Assume that ξ_n can be represented in the form

$$\xi_n = \gamma_n \alpha_n + (1 - \gamma_n)\beta_n, \tag{9}$$

where α_n and β_n are independent and have normal distributions with parameters m_1, σ_1 and m_0, σ_0, respectively, $m_1 > m_0$. The values of γ_n do not depend on α_n and β_n. For relatively long periods of time γ_n take the value 1, which is replaced by short periods when γ_n takes the value 0. The moments when the sequence γ_n enters state 0 are called jumps of the sequence $\{\xi_i, i = 1, 2, \dots\}$ downward, and the moments when the sequence γ_n enters state 1 are referred to as jumps of the sequence $\{\xi_i, i = 1, 2, \dots\}$ in upward direction. At these points in time, periods of a sharp decrease in the values of the measured quantities begin and end specifying the beginning and end of the blockage.

Consider the measure S defined by

$$S = \frac{\sigma_1 m_0 + \sigma_0 m_1}{\sigma_1 + \sigma_0}. \tag{10}$$

For S the following holds true

$$P\{\alpha_k < S\} = \Phi\left(\frac{S - m_1}{\sigma_1}\right),$$
$$P\{\beta_k > S\} = 1 - \Phi\left(\frac{S - m_0}{\sigma_0}\right) = \Phi\left(\frac{m_0 - S}{\sigma_0}\right), \tag{11}$$

where Φ is the Laplace function.

Hence, for the parameter defined by (10), we have

$$P\{\alpha_k < S\} = P\{\beta_k > S\} = E, \tag{12}$$
$$P\{\alpha_k > S\} = P\{\beta_k < S\} = 1 - E,$$

where $E = \Phi((m_0 - m_1)/(\sigma_1 + \sigma_0))$.

If for some numbers in sequence $\{\xi_i, i = 1, 2, \dots\}$ inequalities $\xi_n > S$ and $\xi_{n+1} < S$ hold, then the time instant $n + 1$ is considered as the moment of the jump down. Alternatively, if for values m and $m + 1$ inequalities $x_m < S$ and $x_{m+1} > S$ are valid, then time instant $m + 1$ is considered the moment of the upward jump.

Assuming that γ_n is covariance stationary and denoting

$$P\{\gamma_n = 1\} = p,$$
$$P\{\gamma_n = 0\} = q,$$
$$P\{\gamma_{n+1} = 0 | \gamma_n = 1\} = \phi,$$
$$P\{\gamma_{n+1} = 1 | \gamma_n = 0\} = \psi, \tag{13}$$

the parameters (p, q, ϕ, ψ) are related as follows

$$p = \frac{\psi}{\varphi + \psi},\ q = \frac{\varphi}{\varphi + \psi}. \tag{14}$$

By utilizing this notation, the probability g that inequalities $\xi_n > S$ and $\xi_{n+1} < S$ are both satisfied at the moment $n + 1$ and thus there is a jump downward (blockage) is given by

$$g = P\{\gamma_n = 1, \gamma_{n+1} = 0 | \xi_n > S, \xi_{n+1} < S\} =$$
$$= \frac{P\{\gamma_n = 1, \gamma_{n+1} = 0, \xi_n > S, \xi_{n+1} < S\}}{P\{\xi_n > S, \xi_{n+1} < S\}} =$$
$$= \frac{P\{\gamma_n = 1, \gamma_{n+1} = 0, \xi_n > S, \xi_{n+1} < S\}}{\sum_{i=0}^{1}\sum_{j=0}^{1} P\{\gamma_n = i, \gamma_{n+1} = j, \xi_n > S, \xi_{n+1} < S\}} =$$
$$= \frac{p\phi\overline{E}^2}{q(1-\psi)\overline{E}E + q\psi E^2 + p\phi\overline{E}^2 + p(1-\phi)\overline{E}E}, \tag{15}$$

where $\overline{E} = 1 - E$.

We also note that the following value

$$\overline{q} = \frac{Eq(1-\psi)\overline{E} + q\psi E + p\phi\overline{E}}{p\phi\overline{E}^2 q(1-\psi)\overline{E}E + q\psi E^2 + p\phi\overline{E}^2 + p\phi\overline{E}E}, \tag{16}$$

provides the probability that the decision about blockage taken based on inequalities $x_n > S$ and $x_{n+1} < S$ is erroneous. It follows that the stronger the difference between the mean values of α_n and β_n and the smaller their variance, the more accurately the moments of jumps of γ_n are determined.

5.3. Alternative algorithms

In the numerical results section, we will compare the performance of the proposed algorithm with the results of the ML approaches reported for the millimeter waves application [19–21], see Section 2. On top of this we consider two simple methods, threshold-based and exponentially-weighted moving average (EWMA), briefly described below.

The simplest form of change-point detection is the threshold-based algorithm, where a blockage is detected when RSS falls below a given threshold, R_T. This test is utilized as an extreme case since it is inherently vulnerable to fading phenomena and may potentially result in many false alarms.

The problem of change-point statistical tests is that they often require observations to be realizations of independently and identically distributed random variables. However, RSS observations are not necessarily independent, but can be correlated. Autocorrelation makes classic control charts less sensitive to changes in the mean value [34]. In what follows we utilize the EWMA control chart for autocorrelated data.

Let $\{\xi_i, i = 1, 2, \dots\}$ be a sequence of RSS observations. The value of EWMA statistic at the time n, denoted by L_{ξ_n}, is given by

$$L_\xi(n) = \gamma\xi(n) + (1-\gamma)L_\xi(n-1), \tag{17}$$

The first value of EWMA statistics, $L_\xi(0)$, is usually set to the mean of $\{\xi_i, i = 1, 2, \dots\}$ or, if unknown, to the estimate of mean collected over first K observations. Further, observe that (17) defines a new stochastic process as a function of initial observations and this process has different statistical characteristics compared to those of $\{\xi_i, i = 1, 2, \dots\}$. Given that $L_\xi(0) = E[\xi]$, the mean of the process is provided by

$$E[L_\xi] = E[\xi](1-(1-\gamma)n) + (1-\gamma)nE[\xi], \tag{18}$$

that converges to constant $E[L_\xi] = E[\xi] = \mu_\xi$ as $n \to \infty$, while the variance of $L_{\xi_n}, n = 0, 1, \dots$ is given by

$$\sigma^2[L_\xi] = \sigma^2[\xi]\left(\frac{\gamma}{2-\gamma}\right)(1-(1-\gamma)^{2n}). \tag{19}$$

Thus, control limits for EWMA charts are

$$E[\xi] \pm k\sigma[\xi]\sqrt{\left(\frac{\gamma}{2-\gamma}\right)(1-(1-\gamma)^{2n})}, \tag{20}$$

where k is the design parameter.

An out-of-control behavior is signaled, when L_{ξ_n} at some point in time is less than $(E[\xi] - C(n))$. Note that the lower control limits are time-varying in nature. However, when $n \to \infty$ it is easy to show that

$$\lim_{n\to\infty}\left(\frac{\gamma}{2-\gamma}\right)(1-(1-\gamma)^{2n}) = \frac{\gamma}{2-\gamma}, \tag{21}$$

and the control chart takes the form

$$E[\xi] \pm \sigma[\xi]\sqrt{\left(\frac{\gamma}{2-\gamma}\right)}. \tag{22}$$

Let now $\{\xi_i, i = 1, 2, \dots\}$ be a sequence of observations from covariance stationary stochastic process with mean, and variance is given by $K_\xi(1)$, $E[\xi]$, and $\sigma^2[\xi]$. Assume that it can be represented by the first-order autoregressive process (AR) process in the form $\xi(n) = \phi_0 + \phi_1\xi(n-1) + \epsilon_n$. If $L_\xi(0) = E[\xi]$ it is easy to see that $E[L_\xi] = E[\xi] = \mu_\xi$ when $n \to \infty$. In these conditions, the approximation for variance of $\{\xi_i, i = 1, 2, \dots\}$ is [35]

$$\sigma^2[L_\xi] = \sigma^2[\xi]\left(\frac{\gamma}{2-\gamma}\right)\left(\frac{1-\phi_1(1-\gamma)}{1-\phi_1(1-\gamma)}\right), \tag{23}$$

where ϕ_1 is the parameter of AR(1) process.

The control limit for blockage detection is then

$$E[\xi] - k\sigma[\xi]\sqrt{\left(\frac{\gamma}{2-\gamma}\right)\left(\frac{1+\phi_1(1-\gamma)}{1-\phi_1(1-\gamma)}\right)}. \tag{24}$$

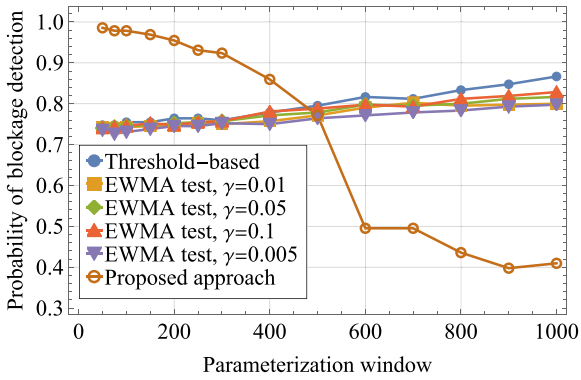

Fig. 12. Blockage detection probability of the considered algorithms.

To parameterize EWMA control charts, a number of parameters have to be provided. First, parameter γ determining the decline of the weights of past observations should be set. The values of k and γ determine the wideness of control belts for a given process with a certain $\sigma^2[\xi]$ and ϕ_1. These two parameters affect the behavior of the so-called average run length (ARL) curve that is usually used to determine the efficiency of a certain change detection procedure. ARL is defined as the average number of observations of the in-control process up to the first out-of-control signal. The ARL is the function of both k and γ. Different parameters of k and γ for a given ARL, $\sigma^2[\xi]$ and ϕ_1 are provided in [34,35]. Finally, μ_ξ $\sigma^2[\xi]$ and ϕ_1 are not usually known in practice and must be estimated from empirical data during the warm-up period of length K.

5.4. Numerical results

In this section, we elaborate on numerical results for blockage detection tests. Specifically, we compare the three approaches introduced in Section 5 and also those ML-based approaches proposed in [19–21,23]. However, differently from those studies, we utilize three metrics for the performance assessment of the proposed tests. These are: (i) blockage detection probability, (ii) latency of blockage detection and (iii) false alarm rate, i.e. false blockage detection probability. This allows us to identify pitfalls in the proposed techniques and to recommend specific values for blockage detection algorithms.

We start our numerical assessment and comparison of algorithms with Fig. 12 showing the blockage detection probability as a function of the parameterization window K and different smoothing constants γ of EWMA test. Recall that the time resolution is 0.05 ms. Note that for the threshold-based test the detection threshold has been set to 15% of the received signal during the parameterization window. As one may observe, both the threshold-based and EWMA tests are characterized by the same behavior — the blockage detection probability increases as K increases. However, for all considered parameters, the blockage detection probability never reaches 0.9 even for unacceptably large value of $K = 1000$ (50 ms). Contrarily, the proposed approach is characterized by the plateauing blockage probability for small values of K (50–150 measurements corresponding to 2.5–7.5 ms) at approximately $p = 0.96 \sim 0.98$. However, as K further increases and the more noise is added to the estimator, the blockage detection probability decreases. Thus, from the blockage probability point of view the proposed approach provides significant gains as compared to other considered techniques.

Blockage probability alone is not a sufficient indicator of the algorithm performance. Specifically, if the blockage is detected too late, this information cannot be utilized at UE or BS sides to take appropriate actions, i.e. proactively changing the MCS. To this aim, Fig. 13 shows the detection delay as a function of the parameterization window.

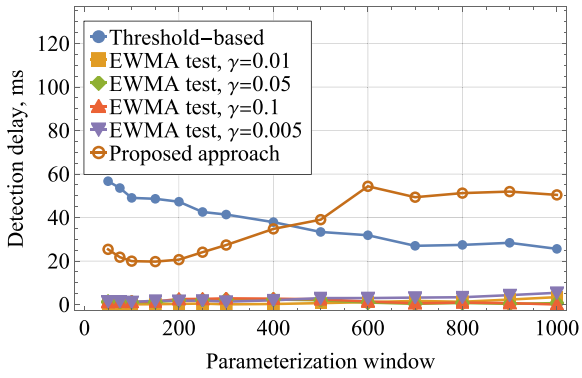

Fig. 13. Detection delay of the considered algorithms.

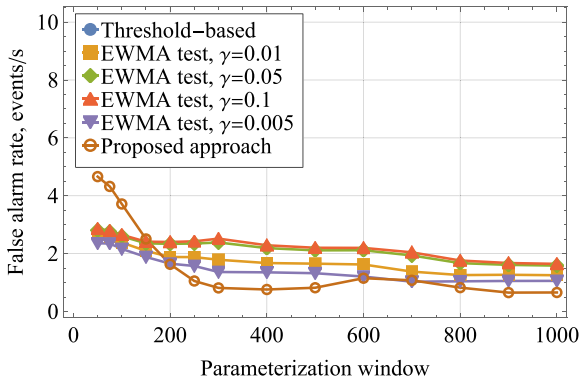

Fig. 14. False alarm rate of the considered algorithms.

Here, the EWMA test for all of the considered constants smoothing γ is characterized by outstanding delay performance by virtually keeping it close to zero. Furthermore, for this test, it is almost independent of the parameterization window performing equally across the considered range of K. The threshold-based test and the proposed test are characterized by much higher detection delay on the order of $K = 20$–60 measurements (1–3 ms). Nevertheless, it is still much less than the fall time, which is on the order of 50–100 ms, see Figs. 10(a) and 10(c), allowing to timely detect the blockage events. Importantly, the proposed test has a local minimum at the value of $K = 75$–150 measurements that coincides with the region of best blockage detection probability, see Fig. 12 making it a suitable candidate for online blockage detection.

The other parameter that is often overlooked in performance evaluation of online blockage detection tests is the false alarm rate, defined as the intensity of false blockage detection. We demonstrate it in Fig. 14 for the considered algorithms. Here, we observe that both threshold-based and EWMA tests perform qualitatively similar having a decrease trend in K. Nevertheless, they still generate, on average, two false blockage events per second of channel monitoring. The proposed test is characterized by more complex behavior. First, at the low value of $K = 75$–150 corresponding to the best detection and delay performance it generates 3–5 false blockage events per second. Then, the false alarm rate quickly decreases to 1 false blockage even per second eventually outperforming the rest of the tests starting from $K = 200$ (10 ms).

By summing up our observations together, we see that the proposed approach is the only one out of the considered tests that has a set of parameters, where the blockage detection probability approaches 1. Importantly, it happens in the region of low values of K minimizing the fraction of time the channel remains without control. While the detection delay for the considered time resolution of 0.05 ms stays within acceptable limits providing the capability to proactively detect blockage events (1–3 ms), the identified region is characterized by a high false alarm rate. Nevertheless, for the considered time resolution the choice of $K = 75$–150 measurements (3.75–7.5 ms) allows to detect blockage with 1–3 ms delay at the expense of 3–5 event/s false alarm rate that can be considered as a viable option for outage-sensitive applications. The value of K minimizing the false alarm rate at approximately 1 event/s is $K = 300$ (15 ms) resulting in a blockage detection probability of 0.91, detection delay of 1.25 ms. However, this choice of parameters leaves the channel without control for much longer periods of time.

The complexity of the online blockage detection algorithm strongly depends on the window size. The algorithm complexity does not exceed $O(n)$ in the worst case. In a similar manner, the mean $E[\xi]$ can be calculated with complexity $O(n)$ in the worst case since the EWMA algorithm has an inherent recursive structure.

6. Conclusions

Motivated by the expected utilization of prospective 6G THz technology for indoor entertainment services, in this paper, we provide a comprehensive characterization of human body blockage at carrier frequency of 156 GHz in terms of both mean attenuation and time-dependent metrics. To alleviate the effect of blockage, we proceed to compare and evaluate the set of blockage detection algorithms. We also report a propagation model accounting for human body blockage.

Our numerical results show that short Tx-to-Rx distances at lower-than-head level of LoS produce high attenuation (15 dB) while for larger distances and higher heights the attenuation is smaller (8–10 dB) and is independent of Tx-to-Rx and blocker-to-Rx distances. Furthermore, there is no drastic difference in blockage duration for different Tx-to-Rx and blocker-to-Rx distances: experiment yields that it varies within 5%–10% of the nominal value in the range of 360–390 ms. Signal fall and rise times are increasing functions of Tx-to-Rx distance (60 ms for 3 m, 80 ms for 5 m and 100 ms for 7 m), but remain quantitatively unchanged for different LoS heights.

We demonstrate that the proposed blockage detection algorithm is the only one out of the considered tests providing the blockage detection probability in the range of 0.96–0.98 and detection latency of 1–3 ms which is similar to state-of-the-art ML-based detection algorithms. In spite of this happening at the high false alarm rate of 3–5 event/s, this approach can be utilized to safely detect blockage for outage sensitive applications. By extending the parameterization period to 15 ms, one minimizes the false alarm rate to just 1 event/s at the expense of decreased blockage detection probability lowering it down to 0.91.

CRediT authorship contribution statement

Alexander Shurakov: Methodology, Validation, Writing – original draft, Writing – review & editing, Visualization. **Dmitri Moltchanov:** Conceptualization, Methodology, Validation, Data curation, Software, Writing – original draft, Writing – review & editing. **Anatoliy Prikhodko:** Investigation, Resources. **Abdukodir Khakimov:** Formal analysis, Writing – original draft. **Evgeny Mokrov:** Formal analysis, Writing – original draft, Writing – review & editing. **Vyacheslav Begishev:** Methodology, Validation, Funding acquisition. **Ivan Belikov:** Investigation, Resources. **Yevgeni Koucheryavy:** Validation, Writing – original draft, Writing – review & editing, Project administration. **Gregory Gol'tsman:** Validation, Writing – review & editing, Supervision, Funding acquisition.

Declaration of competing interest

The authors declare that they have no known competing financial interests or personal relationships that could have appeared to influence the work reported in this paper.

Data availability

The authors are unable or have chosen not to specify which data has been used.

Acknowledgments

Sections 1 and 5 were written by Evgeni Mokrov under the support of the Russian Science Foundation, Russia, project no. 22-29-00222. This paper has been supported by the RUDN University Scientific Projects Grant System, project no. 021928-2-074 (recipient is Vyacheslav Begishev, Section 2). Section 3 was written by Alexander Shurakov under the support of the Russian Science Foundation, Russia, project no. 21-72-10119. The research leading to the results presented in Sections 4 and 6 has received funding from the Basic Research Program at the National Research University Higher School of Economics, Russia (recipient is Gregory Gol'tsman).

References

[1] T.S. Rappaport, Y. Xing, O. Kanhere, S. Ju, A. Madanayake, S. Mandal, A. Alkhateeb, G.C. Trichopoulos, Wireless communications and applications above 100 GHz: Opportunities and challenges for 6G and beyond, IEEE Access 7 (2019) 78729–78757.

[2] V. Petrov, T. Kurner, I. Hosako, IEEE 802.15. 3d: First standardization efforts for sub-terahertz band communications toward 6G, IEEE Commun. Mag. 58 (11) (2020) 28–33.

[3] J.M. Jornet, I.F. Akyildiz, Channel modeling and capacity analysis for electromagnetic wireless nanonetworks in the terahertz band, IEEE Trans. Wireless Commun. 10 (10) (2011) 3211–3221.

[4] I.F. Akyildiz, J.M. Jornet, Realizing ultra-massive MIMO (1024x1024) communication in the (0.06–10) terahertz band, Nano Commun. Netw. 8 (2016) 46–54.

[5] V. Petrov, M. Komarov, D. Moltchanov, J.M. Jornet, Y. Koucheryavy, Interference and SINR in millimeter wave and terahertz communication systems with blocking and directional antennas, IEEE Trans. Wireless Commun. 16 (3) (2017) 1791–1808.

[6] N. Stepanov, D. Moltchanov, V. Begishev, A. Turlikov, Y. Koucheryavy, Statistical analysis and modeling of user micromobility for THz cellular communications, IEEE Trans. Veh. Technol. (2021).

[7] V. Petrov, D. Moltchanov, Y. Koucheryavy, J.M. Jornet, Capacity and outage of terahertz communications with user micro-mobility and beam misalignment, IEEE Trans. Veh. Technol. 69 (6) (2020) 6822–6827.

[8] D. Moltchanov, Y. Gaidamaka, D. Ostrikova, V. Beschastnyi, Y. Koucheryavy, K. Samouylov, Ergodic outage and capacity of terahertz systems under micromobility and blockage impairments, IEEE Trans. Wireless Commun. (2021).

[9] Y. Xing, T.S. Rappaport, Propagation measurement system and approach at 140 GHz-moving to 6G and above 100 GHz, in: 2018 IEEE Global Communications Conference, GLOBECOM, IEEE, 2018, pp. 1–6.

[10] J.M. Eckhardt, V. Petrov, D. Moltchanov, Y. Koucheryavy, T. Kürner, Channel measurements and modeling for low-terahertz band vehicular communications, IEEE J. Sel. Areas Commun. 39 (6) (2021) 1590–1603.

[11] V. Petrov, J.M. Eckhardt, D. Moltchanov, Y. Koucheryavy, T. Kurner, Measurements of reflection and penetration losses in low terahertz band vehicular communications, in: 2020 14th European Conference on Antennas and Propagation (EuCAP), IEEE, 2020, pp. 1–5.

[12] Y. Xing, T.S. Rappaport, Propagation measurement system and approach at 140 GHz-moving to 6G and above 100 GHz, in: 2018 IEEE Global Communications Conference, GLOBECOM, IEEE, 2018, pp. 1–6.

[13] K. Du, O. Ozdemir, F. Erden, I. Guvenc, Sub-terahertz and mmwave penetration loss measurements for indoor environments, 2021, arXiv preprint arXiv:2103.02745.

[14] J. Kokkoniemi, J. Lehtomäki, V. Petrov, D. Moltchanov, M. Juntti, Frequency domain penetration loss in the terahertz band, in: 2016 Global Symposium on Millimeter Waves (GSMM) & ESA Workshop on Millimetre-Wave Technology and Applications, IEEE, 2016, pp. 1–4.

[15] B.A. Bilgin, H. Ramezani, O.B. Akan, Human blockage model for indoor terahertz band communication, in: 2019 IEEE International Conference on Communications Workshops (ICC Workshops), IEEE, 2019, pp. 1–6.

[16] Y. Wu, J. Kokkoniemi, C. Han, M. Juntti, Interference and coverage analysis for terahertz networks with indoor blockage effects and line-of-sight access point association, IEEE Trans. Wireless Commun. 20 (3) (2020) 1472–1486.

[17] A. Shafie, N. Yang, S. Durrani, X. Zhou, C. Han, M. Juntti, Coverage analysis for 3D terahertz communication systems, IEEE J. Sel. Areas Commun. 39 (6) (2021) 1817–1832.

[18] A. Bonfante, L.G. Giordano, I. Macaluso, N. Marchetti, Performance of predictive indoor mmwave networks with dynamic blockers, IEEE Trans. Cognitive Comm. and Netw. (2021).

[19] S. Moon, H. Kim, Y.-H. You, C.H. Kim, I. Hwang, Deep neural network for beam and blockage prediction in 3GPP-based indoor hotspot environments, Wirel. Pers. Commun. (2022) 1–20.

[20] T. Gu, Z. Fang, Z. Yang, P. Hu, P. Mohapatra, Mmsense: Multi-person detection and identification via mmwave sensing, in: Proceedings of the 3rd ACM Workshop on Millimeter-Wave Networks and Sensing Systems, 2019, pp. 45–50.

[21] M. Alrabeiah, A. Alkhateeb, Deep learning for mmwave beam and blockage prediction using sub-6 GHz channels, IEEE Trans. Commun. 68 (9) (2020) 5504–5518.

[22] ITU-R, Propagation data and prediction methods required for the design of terrestrial line-of-sight systems, ITU-R P 530-17, ITU, 2017.

[23] S. Wu, M. Alrabeiah, A. Hredzak, C. Chakrabarti, A. Alkhateeb, Deep learning for moving blockage prediction using real millimeter wave measurements, 2021, arXiv preprint arXiv:2101.06886.

[24] A. Shurakov, I. Belikov, A. Prikhodko, D. Mikhailov, G. Gol'tsman, Membrane-integrated planar Schottky diodes for waveguide mm-wave detectors, Microw. Telecommun. Technol. 3 (2021) 34.

[25] 3GPP, Study on channel model for frequencies from 0.5 to 100 GHz (Release 14), 3GPP TR 38.901 V14.1.1, 3GPP, 2017.

[26] G.R. MacCartney, T.S. Rappaport, S. Rangan, Rapid fading due to human blockage in pedestrian crowds at 5G millimeter-wave frequencies, in: GLOBECOM 2017-2017 IEEE Global Communications Conference, IEEE, 2017, pp. 1–7.

[27] G.R. MacCartney, S. Deng, S. Sun, T.S. Rappaport, Millimeter-wave human blockage at 73 GHz with a simple double knife-edge diffraction model and extension for directional antennas, in: 2016 IEEE 84th Vehicular Technology Conference (VTC-Fall), IEEE, 2016, pp. 1–6.

[28] M. Gapeyenko, A. Samuylov, M. Gerasimenko, D. Moltchanov, S. Singh, E. Aryafar, S.-p. Yeh, N. Himayat, S. Andreev, Y. Koucheryavy, Analysis of human-body blockage in urban millimeter-wave cellular communications, in: 2016 IEEE International Conference on Communications, ICC, IEEE, 2016, pp. 1–7.

[29] T.S. Rappaport, et al., Wireless Communications: Principles and Practice, vol. 2, prentice hall PTR New Jersey, 1996.

[30] 3GPP, Technical Specification Group Radio Access Network; Study on Channel Model for Frequency Spectrum above 6 GHz (Release 16), Tech. rep., 3GPP TR 38.900 V16.1.0, 2020.

[31] P. Boronin, V. Petrov, D. Moltchanov, Y. Koucheryavy, J.M. Jornet, Capacity and throughput analysis of nanoscale machine communication through transparency windows in the terahertz band, Nano Commun. Netw. 5 (3) (2014) 72–82.

[32] 3GPP, NR; Multi-connectivity; Stage 2 (Release 16), 3GPP TS 37.340 V16.0.0, 3GPP, 2019.

[33] A.S. Polunchenko, A.G. Tartakovsky, State-of-the-art in sequential change-point detection, Methodol. Comput. Appl. Probab. 14 (3) (2012) 649–684.

[34] J.E. Wieringa, et al., Statistical Process Control for Serially Correlated Data, Labyrint Publication, 1999.

[35] J.E. Wieringa, et al., Control charts for monitoring the mean of AR (1) data, University of Groningen, 1998.